WARWICK
THE UNIVERSITY OF WARWICK

Original citation:
Vasdravellis, George, Baiguera , M. and Karavasilis, Theodore L.. (2016) Dual seismic-resistant steel frame with high post-yield stiffness braces for residual drift reduction : numerical evaluation. Journal of Constructional Steel Research, 12 . pp. 198-212.
Permanent WRAP URL:
http://wrap.warwick.ac.uk/78017

Copyright and reuse:
The Warwick Research Archive Portal (WRAP) makes this work by researchers of the University of Warwick available open access under the following conditions. Copyright © and all moral rights to the version of the paper presented here belong to the individual author(s) and/or other copyright owners. To the extent reasonable and practicable the material made available in WRAP has been checked for eligibility before being made available.

Copies of full items can be used for personal research or study, educational, or not-for-profit purposes without prior permission or charge. Provided that the authors, title and full bibliographic details are credited, a hyperlink and/or URL is given for the original metadata page and the content is not changed in any way.

Publisher's statement:
© 2016, Elsevier. Licensed under the Creative Commons Attribution-NonCommercial-NoDerivatives 4.0 International http://creativecommons.org/licenses/by-nc-nd/4.0/

A note on versions:
The version presented here may differ from the published version or, version of record, if you wish to cite this item you are advised to consult the publisher's version. Please see the 'permanent WRAP URL' above for details on accessing the published version and note that access may require a subscription.

For more information, please contact the WRAP Team at: wrap@warwick.ac.uk

warwick.ac.uk/lib-publications

Dual seismic-resistant steel frame with high post-yield stiffness energy-dissipative braces for residual drift reduction

Marco Baiguera*, George Vasdravellis* and Theodore L. Karavasilis**

* Institute for Infrastructure and Environment, Heriot-Watt University, Edinburgh EH14 4AS, United Kingdom

e-mails: mb311@hw.ac.uk, G.Vasdravellis@hw.ac.uk

** School of Engineering, University of Warwick, Coventry CV4 7AL, United Kingdom

e-mail: T.Karavasilis@warwick.ac.uk

Keywords: Dual seismic-resistant steel frame; low-damage steel frame; residual drift mitigation; energy-dissipative brace; replaceable fuse; nonlinear finite element analysis.

Abstract. A dual seismic-resistant steel frame, which consists of a moment-resisting frame equipped with high post-yield stiffness energy-dissipative braces, is proposed and numerically evaluated. Replaceable hourglass shape pins made of duplex stainless steel with high post-yield stiffness and large energy dissipation and fracture capacity are in series connected to conventional steel braces. Moreover, replaceable fuses are introduced in the beams at the locations where plastic hinges are expected to develop. A performance-based seismic design procedure and appropriate capacity design rules are used to design the dual frame, while its seismic performance is evaluated with advanced numerical simulations using experimentally validated shell-solid finite element models and simplified beam element models. The numerical results show that the dual frame has adequate stiffness and energy dissipation capacity to control peak storey drifts (i.e. non-structural damage), while plastic deformations (i.e. structural damage) are isolated within the replaceable pins of the braces and the beam fuses. In addition, the high post-yield stiffness of the pins, combined with the appreciable elastic deformation capacity of the moment-resisting frame, results in significant reduction of residual storey drifts, which are found to have a mean value of 0.06% under the design earthquake and a mean value of 0.12% under the maximum considered earthquake. These values indicate a superior residual storey drift performance compared to steel frames equipped with buckling restrained braces, and highlight the potential of the proposed dual frame to help steel buildings to return to service within an acceptable short time in the aftermath of a strong earthquake.

1 INTRODUCTION

Conventional seismic-resistant steel frames designed according to current seismic provisions, e.g. Eurocode 8 [1], prevent collapse and ensure life safety under the design earthquake. However, two major drawbacks of conventional systems are that they experience significant inelastic deformations (i.e. damage) in main structural members and residual storey drifts after a strong seismic event. Socio-economic losses associated with repairing damage in structural members include high repair costs and excessive disruption to building use or occupation. Residual storey drifts may pose further complications: a recent study on the economic impact of residual drifts showed that direct and indirect repair costs are not financially viable when residual drifts are greater than 0.5% [2, 3].

Braced frames represent a system with enhanced seismic performance due to their high initial stiffness, which can effectively reduce storey drifts. However, conventional braced frames, such as concentrically braced frames (CBFs), exhibit a degrading hysteretic behaviour, which results in damage concentration to certain stories, fracture, and increased collapse potential. Buckling-restrained braced frames (BRBFs) represent an improved class of braced frames [4, 5]. The buckling-restrained braces (BRBs) exhibit a stable hysteretic response and the ability to withstand significant ductility demands. However, they may be susceptible to large residual drifts and damage concentrations due to their low post-yield stiffness [6]. Previous analytical studies have shown that BRBFs designed according to ASCE 7-05 [7] do not meet the immediate occupancy performance level under the design-basis earthquake (10% probability of occurrence in 50 years; denoted as DBE), due to residual drifts greater than 0.5% [8]. Recent experimental and analytical studies on BRBFs [9, 10, 11] have also shown that residual drifts can be as high as 1.3% under the DBE. Kiggins and Uang [12] proposed the introduction of a moment resisting frame (MRF) as a secondary lateral system, which provides a restoring force and results in significant reduction of the residual storey drifts of BRBFs.

An effective strategy to overcome the issue of reparability of structural members is to concentrate damage in carefully designed replaceable elements, typically named in the literature as structural fuses. This concept was first presented by Balut and Gioncu [13] as an alternative to dog-bone connections in MRFs. The fuses are detailed to dissipate energy and to be easily replaced if damaged, whereas the main structural members are designed to be elastic. In addition, the removal and replacement of fuses allows the structure to recenter [14].

Vayas and Thanopoulos [15] proposed and experimentally validated rectangular pins as fuses in CBFs. The role of the pins is to protect the braced members from damage. Gray et al. [16] developed a novel cast steel yielding brace system able to enhance the seismic performance of braced frames and to limit damage to replaceable structural elements. Replaceable nonlinear links in steel MRFs and eccentrically braced frames were proposed by Shen et al. [17] and Mansour et al. [18] respectively, while replaceable welded or bolted plates were used in composite MRFs by Castiglioni et al. [19].

To reduce residual deformations, researchers have proposed the use of post-tensioning technology in MRFs or braced frames. Self-centering MRFs use post-tensioned bars or tendons to clamp the beams on columns while permitting a gap opening in the beam-column interface. Post-tensioned bars provide restoring forces to eliminate residual drifts. Several configurations of self-centering MRFs have been proposed, with the main difference being relevant to the type of energy dissipating device used, i.e. steel yielding based [20-25] or friction based [26-29]. Christopoulos et al. [30] proposed a braced frame using self-centering braces. The braces consist of structural elements interconnected by a friction energy-dissipative mechanism and equipped with pre-tensioned fibre tendons that provide restoring forces. Miller et al. [31] proposed a self-centering BRBF using a typical BRB component and super elastic nickel-titanium shape memory alloy rods. Simpler approaches to mitigate residual drifts have been studied in [32]. Among these, providing high post-yield stiffness is recognized as an effective strategy to reduce residual drifts.

This paper proposes an MRF equipped with concentric braces, denoted as dual CBF-MRF, which uses simple structural details to provide enhanced seismic performance, i.e.: a) energy-dissipative hourglass shape pins made of duplex stainless steel (SSD) with high post-yield stiffness, designated as SSD-WHPs, are placed in series with the concentric braces; and b) replaceable fuses are placed at the locations of the beams where plastic hinges are expected to develop. A prototype building is designed according to the provisions of Eurocodes 3 [33] and 8 [1] using as seismic-resistant system either a BRBF coupled with an MRF (BRBF-MRF) or the proposed CBF-MRF. The seismic performances of the BRBF-MRF and the CBF-MRF are then evaluated using numerical simulations. A detailed solid-shell model and a simplified beam-solid model are constructed for that purpose using the commercial software Abaqus [34]. The hysteretic behaviour of the key components, i.e. the SSD-WHPs and the beam fuses, is calibrated using available experimental results. Monotonic and cyclic nonlinear static analyses, as well as nonlinear dynamic analyses using a set of 22 earthquake records

scaled to three different seismic intensities, are executed and comparisons between the BRBF-MRF and the CBF-MRF are made.

2 STEEL DUAL CBF-MRF

Fig. 1a shows the configuration of the proposed CBF-MRF. The SSD-WHPs are installed only at one end of the braces and pass through aligned holes between the gusset plate and a strong U-shaped plate, which is connected by either welding or bolting to the brace member (Fig. 1b). WHPs are hourglass-shape steel yielding devices that dissipate energy due to bending inelastic deformations. The geometric properties of the bending part of a WHP are shown in Fig. 2a. The internal parts have length L_{WHP}, external diameter D_e, and mid-length diameter D_i. The internal part is assumed to have fixed boundary conditions as it bends. The hourglass shape promotes a constant curvature profile and a uniform distribution of plastic deformations to delay fracture and increase energy dissipation. WHPs have been previously used by Vasdravellis et al. [25] in a post-tensioned connection. Component tests on isolated WHPs conducted in [25] are shown in Fig. 2b. A further experimental evaluation of the cyclic behaviour of WHPs [35] made of high-strength steel and two grades of stainless steel (i.e. austenitic grade 304 and SSD) showed that they have stable hysteresis and high fracture capacity. In that study, SSD-WHPs showed excellent energy dissipation capacity and high post-yield stiffness, indicating the potential benefits of using them in bracing systems.

Replaceable fuses are placed in the main beams immediately after the gusset plates, where plastic hinges are expected to develop, as shown in Fig. 1a. They are designed following the same concept of the replaceable link proposed by Shen et al. [17]. The fuses are smaller than the main beam steel I-sections, welded on strong end plates, which in turn are bolted on the main beam (Fig. 1c).

The proposed frame can be designed to provide: a) high initial stiffness resulting in effective control of storey drifts and, thus, control of damage in drift-sensitive non-structural elements; b) elimination of structural damage by concentrating plastic deformations in the SSD-WHPs and the beam fuses; and c) significant reduction of residual drifts as the result of the high post-yield stiffness of the SSD-WHPs combined with the appreciable elastic deformation capacity of the MRF.

3 PROTOTYPE BUILDING DESIGN AND DETAILING

3.1 Prototype building

Fig. 3a shows the plan view of a 6-storey prototype building with three equal bays in each direction. Seismic resistance is provided by the perimeter frames, whereas the interior frames support gravity loads only. The bay width and the storey height are 6 m and 3 m, respectively. The gravity loads are determined according to Eurocode 1 [36]. The dead load is equal to 5.8 kN/m^2, while the live load is equal to 3.5 kN/m^2 for a typical floor and 1.5 kN/m^2 for the roof. Fig. 3b shows the elevation of a perimeter frame, which is designed either as a BRBF-MRF or as CBF-MRF, according to Eurocode 3 [33] and Eurocode 8 [1].

3.2 Design of the BRBF-MRF

The BRBF-MRF is designed according to the provisions of Eurocode 8 [1] for CBFs with adjustment factors to take into account the strain-hardening of the BRBs for the application of capacity design rules, following the approach recommended by ANSI/AISC 341-10 [37]. The design basis earthquake (DBE) has a return period of 475 years, and it is expressed by the elastic response spectrum of Eurocode 8 [1] with a PGA equal to 0.36 g and soil type B. The steel yield stress for columns, beams, and braces is assumed equal to 275 MPa. Eurocode 8 [1] imposes a serviceability limit on peak storey drifts, $\theta_{s,max}$, under the frequently-occurred earthquake (50% probability of occurrence in 50 years; denoted as FOE). The FOE has intensity equal to 50% of the intensity of the DBE and the limit on $\theta_{s,max}$ is 0.5% and 0.75% for non-ductile and ductile non-structural elements, respectively. Table 1 lists the final sections of the BRBF-MRF, which are found through an iterative design procedure in order to satisfy the storey drift limits and capacity design requirements. The fundamental period of vibration of the structure is 0.77 s, and the estimated maximum values of $\theta_{s,max}$ are 0.48% under the FOE, 0.96% under the DBE, and 1.44 % under the maximum considered earthquake (2% probability of exceedance in 50 years; denoted as MCE). The beam and column sections of the MRF are increased to result in a MRF to BRBF stiffness ratio equal to approximately 0.3, i.e. the MRF contributes 30% to the stiffness of the frame. This results in an overdesign of the beam-column strength ratio (capacity design rule), which is taken into account in the design of the proposed CBF-MRF, as described later.

3.3 Design of the dual CBF-MRF

The proposed CBF-MRF has the same beam and column cross-sections as the BRBF-MRF. The BRBs are replaced by HEA300 sections connected in series to the SSD-WHPs, as shown in Fig. 1.

3.3.1 Design of bracing members with SSD-WHPs

Bracing members with SSD-WHPs are designed to provide initial elastic stiffness and yield force similar to the BRBs of the BRBF-MRF. The mechanical characteristics of the WHPs are predicted by analytical equations derived from plastic analysis and simple mechanics, as described in detail in [25]. The assumed static system for half of a WHP is illustrated in Fig. 2a. The yield force of half of a WHP, V_{WHP}, is controlled either by the plastic moment of resistance, M_{pl}, or the plastic shear resistance, V_{pl} [33]:

$$M_{\mathrm{pl}} = \left(\frac{D_e^3}{6}\right) f_{\mathrm{y,WHP}} \tag{1}$$

$$V_{\mathrm{pl}} = 0.9\frac{\pi D_i^2}{4} f_{\mathrm{y,WHP}}/\sqrt{3} \tag{2}$$

where $f_{\mathrm{y,WHP}}$ is the yield strength of the WHP material. To avoid that the M_{pl} is reached at the ends before the V_{pl} is reached at the mid-length, the following condition must be satisfied:

$$V_{\mathrm{WHP}} = \frac{2M_{\mathrm{pl}}}{L_{\mathrm{WHP}}} < V_{\mathrm{pl}} \tag{3}$$

The yield force of a WHP, $F_{\mathrm{y,WHP}}$, is then calculated as:

$$F_{\mathrm{y,WHP}} = 2V_{\mathrm{WHP}} \tag{4}$$

The elastic stiffness K_{fe} of a WHP is given by:

$$K_{\mathrm{fe}} = 2\beta \frac{9\pi D_{\mathrm{e}}^3 D_{\mathrm{i}} EG}{(40ED_{\mathrm{e}}^2 L_{WHP} + 48GL_{\mathrm{WHP}}^3)} \tag{5}$$

where E is the modulus of elasticity and G is the shear modulus of the WHP material. β is a parameter that accounts for the additional flexibility due to local yielding in the supporting plates observed in the experimental validation [25] and is equal to 0.6. In the proposed system, n_{WHP} WHPs are placed in series with the brace, and therefore, the yield force $F_{\mathrm{y,tot}}$ and the global stiffness K_{tot} of the energy-dissipative braces are calculated as follows:

$$F_{\mathrm{y,tot}} = n_{\mathrm{WHP}} \cdot F_{\mathrm{y,WHP}} \tag{6}$$

$$\frac{1}{K_{\mathrm{tot}}} = \frac{1}{K_{\mathrm{WHPs}}} + \frac{1}{K_{\mathrm{brace}}} = \frac{1}{n_{\mathrm{WHP}} \cdot K_{\mathrm{fe}}} + \frac{1}{\frac{EA_{\mathrm{brace}}}{L_{\mathrm{brace}}}} \tag{7}$$

where K_{WHPs} is the stiffness of all WHPs, and K_{brace} is the stiffness of the bracing member having length L_{brace} and cross-sectional area A_{brace}.

Using the above equations, the SSD-WHPs are designed so that the CBF-MRF has a fundamental period of vibration equal to 0.75 s., i.e. comparable to that of the BRBF-MRF. The SSD material has a yield strength equal to 560 MPa. Table 2 lists the design details of the CBF-MRF. Braces have strong HEA300 sections to ensure that the SSD-WHPs will yield first.

The CBF-MRF is expected to exhibit high post-yield stiffness as a result of the SSD material behaviour. To meet capacity design requirements and avoid undesirable column failures due to high post-yield stiffness, friction pads are placed between the brace members and the beam gusset plate at the top of each floor, as indicated in Fig. 1. The friction pad is activated, i.e. it 'yields', at a predefined story drift level and it has an elastic perfectly plastic force-displacement behaviour in order to ensure that the structure meets the capacity design requirements. The predefined storey drift level in the present frame is 3%, as identified by the nonlinear pushover analysis. i.e. two times larger than the drift expected under the MCE.

3.3.2 Beam fuse design

The replaceable end-plate link concept proposed by Shen et al. [17] is considered for the design of the beam fuse. Fig. 4 shows the geometric details of the beam fuse where the beam is weakened at a distance *S* from the column face. Plastic deformations are intended to concentrate at the beam fuse, thus protecting the beam and the beam-column connection from yielding. The beam fuse is designed according to the procedure presented in [17]. The

geometry of the beam fuse is defined by the length l_{fuse}, the distance from the gusset plate a, and the fuse depth d_{fuse}. The beam fuse size is subject to the limits expressed by:

$$0.5\ b_{\text{beam}} \leq a \leq 0.75\ b_{\text{beam}} \tag{8}$$

$$0.65\ d_{\text{fuse}} \leq l_{\text{fuse}} \leq 0.85\ d_{\text{fuse}} \tag{9}$$

where b_{beam} is the width of the main beam section.

Limits on the plastic moment ratio for the beam fuse are defined on the basis of limits on the flange cut recommended for RBS connections in [38]. The limits on the plastic moment ratio are:

$$0.6 \leq \frac{M_{\text{pl,fuse}}}{M_{\text{pl,beam}}} \leq 0.85 \tag{10}$$

where $M_{\text{pl,fuse}}$ and $M_{\text{pl,beam}}$ are the plastic moments of the beam fuse and the main beam, respectively.

The maximum moment at the face of the column, $M_{\text{max,col}}$, must satisfy the condition:

$$M_{\text{max,col}} = \frac{L}{L-S} M_{\text{pl,fuse}} \leq M_{\text{pl,beam}} \tag{11}$$

where L is half the beam length. The above design procedure results in IPE270 sections for the beam fuses on each floor of the prototype building. Table 3 gives the geometric details of the beam fuse.

3.3.3 WHP – gusset plate connection design

The thickness of the lower gusset plates and the U-shaped plates (Fig. 1b) is determined according to the design rules presented in [35]. In order to resist the bearing force $F_{\text{y,WHP}}$ from an SSD-WHP without yielding, the minimum required thickness of the gusset plates $t_{\text{gus,min}}$ and U-shaped plates $t_{\text{sp,min}}$ are given by:

$$t_{\mathrm{gus,min}} = \frac{0.35\, F_{\mathrm{y,WHP}} E}{f_{\mathrm{y,gus}}^2 k_{\mathrm{d}}} \tag{12}$$

$$t_{\mathrm{sp,min}} = \frac{3{,}546\, M_{\mathrm{pl}}}{(38{,}809\, F_{\mathrm{y,WHP}}^2 + 40\, M_{\mathrm{pl}} k_{\mathrm{d}} f_{\mathrm{y,sp}})^{0.5} - 197\, F_{\mathrm{y,WHP}}} \tag{13}$$

where $f_{\mathrm{y,gus}}$ and $f_{\mathrm{y,sp}}$ are the yield strengths of the gusset plate and the U-shaped plate (300 MPa), respectively. k_{d} is a factor accounting for the clearance between the SSD-WHPs and the drilled holes in the U-shaped plates [35]. In addition, the gusset and U-shaped plates are verified against buckling by using the strip column method proposed by Thornton [39]. The design results in gusset plates with thickness equal to 40 mm and U-shaped plates with thickness equal to 50 mm. The top gusset plates, i.e. those at the connection of the braces with the beam of the upper floor, are designed using the Eurocode 3 [33] procedure, which results in 40 mm thick plates.

4 NONLINEAR FINITE ELEMENT MODELS

The seismic performance of the proposed CBF-MRF is studied by means of nonlinear finite element (FEM) analyses using the Abaqus software [34]. A detailed three-dimensional model, based on the use of solid and shell elements, is constructed to study both the local and global behaviour of the system and to identify all possible failure modes through nonlinear monotonic and cyclic pushover analyses. A simplified version of the detailed model, based on the use of beam elements, is also created to evaluate the global seismic response of the structure through nonlinear dynamic analyses. Friction pads are modelled only in the simplified model, since the detailed model is intended to verify the former for roof drifts up to 3% (i.e. the drift level at which the friction pads yield).

4.1 Detailed solid-shell FEM model

Fig. 5 shows an overview of the detailed FEM model. The geometry of the central bay of the prototype building perimeter frame (see Fig. 3) is reproduced in full detail. To reduce computational time, both solid and shell elements are adopted. Beams, columns and bracing members are modelled using shell elements with reduced integration, namely S4R in Abaqus. The SSD-WHPs, gusset plates, U-shaped plates and beam fuses are modelled using solid elements with reduced integration, namely C3D8R. Solid-shell coupling constraints are used to allow for the correct transition of stresses between shell and solid elements. To account for

P-Δ effects from the gravity frame of the prototype building, a lean-on column is added and truss elements are used to link it to the frame. The moment of inertia and area of the lean-on column are the sum of the moments of inertia and areas of all gravity columns. Fig. 6a shows the mesh discretization used. The mesh density in the regions of the frame where plastic deformations are expected to develop, i.e. the WHP-gusset plate connections and the beam fuses, is defined by creating sub-models of these regions and calibrating the modelling parameters against previous experimental studies, as will be described later.

Surface-based tie constraints, which impose equal displacements among the nodes of two surfaces, are defined between all welded regions, i.e. the beam-column connections, the end-plates welded to the beam fuses, the U-shaped plates welded to the bracing members, and the gusset plates welded to the beam and column flanges, as indicated in Fig. 6b. Surface-to-surface contact interactions are defined between the external surfaces of the SSD-WHPs and the holes of the U-shaped plates and gusset plates. This requires the definition of a master and a slave contact surface. The choice of the master and slave surface is made considering the mesh discretization, i.e. the surface with the coarser mesh was chosen as master surface because it results in a smoother solution [34]. A contact property with normal and tangential behaviour is defined, assigning a friction coefficient of 0.2. The diaphragm action of the slab is simulated by a linear equation constraint, imposing equal horizontal displacements on the nodes of the top flanges of the beam.

The yield stress of the main structural members is 275 MPa and the yield stress of the SSD material is 560 MPa. An elastoplastic material with isotropic hardening behaviour is defined for the main structural members.

4.1.1 Calibration of cyclic hardening parameters for SSD-WHPs

The material properties of the SSD-WHPs are calibrated using the experimental results reported in [35]. In that study, several cyclic tests on SSD-WHPs were carried out using the testing apparatus shown in Fig. 2b. Fig. 7a shows the three-dimensional FEM model that was used to simulate the hysteretic response of WHPs made of high-strength steel in [40]. Those models are modified in this study to capture the behaviour of SSD material. Only half of the WHP is modelled due to its symmetric geometry. Both the WHP and the supporting plates are discretized using C3D8R elements. In order to capture the pinching behaviour at zero force observed in the experimental curve (Fig. 7b) due to the slip of WHPs within the surrounding holes, a small clearance, equal to 0.1 mm, is left between the cylindrical external surfaces and the holes of the U-shaped plates, where surface-to-surface contact interactions are defined.

The cyclic loading protocol described in ANSI/AISC 341-10 [37] is applied to reproduce the corresponding test in [35]. Displacement-controlled analysis is conducted under quasi-static loading conditions in the large displacement/strain nonlinear regime, along with automatic stabilization in order to overcome numerical issues related to the contact interactions.

The hysteretic behaviour of SSD-WHPs is simulated by an elastoplastic material model with combined isotropic and kinematic hardening. The material model is defined by the yield surface $\varphi(\boldsymbol{\sigma})$ defined as [34]:

$$\varphi(\boldsymbol{\sigma}) = \sqrt{\frac{3}{2}(\boldsymbol{S}-\boldsymbol{\alpha})^t(\boldsymbol{S}-\boldsymbol{\alpha})} - \sigma^0 \tag{14}$$

where σ^0 is the yield stress, t is the transposition operation, $\boldsymbol{S}$ is the stress deviator, $\boldsymbol{\sigma}$ is the stress vector and $\boldsymbol{\alpha}$ is the backstress vector. The hardening laws for each backstress are defined as:

$$\boldsymbol{\alpha} = \sum_{\mathrm{k}=1}^{\mathrm{B}} \boldsymbol{\alpha}_{\mathrm{k}} \tag{15}$$

$$\dot{\boldsymbol{\alpha}}_{\mathrm{k}} = \frac{C_{\mathrm{k}}}{\sigma^0}(\boldsymbol{\sigma}-\boldsymbol{\alpha})\,\dot{\bar{\varepsilon}}^p - \gamma_{\mathrm{k}}\,\boldsymbol{\alpha}_{\mathrm{k}}\,\dot{\bar{\varepsilon}}^p \tag{16}$$

where a superimposed dot indicates an incremental quantity, B is the total number of the backstresses, C_{k} and γ_{k} are the constitutive material parameters to be calibrated against the experimental results, and $\dot{\bar{\varepsilon}}^p$ is the equivalent plastic strain rate. Fig. 7b shows that a good agreement is found with the experimental cyclic force-displacement curve reported in [35] using the following parameters: B= 1, σ^0= 500 MPa, C_1= 11,000 MPa, and γ_1= 40.

4.1.2 Calibration of cyclic hardening parameters for the beam fuse

To ensure that the numerical model for the fuse is reliable and capable of capturing the deterioration of stiffness and strength due to buckling phenomena, the material parameters are calibrated against the experimental results of full-scale tests on a beam-column connection with a replaceable link reported by Shen et al. [17]. The tested specimen is reproduced in Abaqus using the same modelling features as for the whole frame model, i.e. shell (S4R) elements for the beam and column, and solid (C3D8R) elements for the fuse. Similar to the calibration procedure presented in the previous section, the constitutive material parameters of the fuse are identified iteratively by conducting several simulations. Fig. 8a shows that the

FEM model is capable of capturing the buckling of the replaceable link and Fig. 8b shows that a good correlation between the experimental and the numerical results is achieved adopting the following parameters: B= 1, σ^0= 390 MPa, C_1= 4,000 MPa, and γ_1= 80.

4.2 Simplified beam-solid FEM model

The central bay of the prototype building perimeter frame is modelled using a simplified modelling approach and the response is compared against the pushover results of the detailed model. In the simplified version of the numerical model, beams and columns are modelled using two-node linear beam elements, namely B31 in Abaqus. A lean-on column is added to the frame to account for P-Δ effects from the gravity frame using the same modelling features described for the detailed model. Fig. 9 shows the simplified model, with a detailed view of the second storey. Beam-column and brace-beam connections are modelled using appropriate multi-point constraints. The diaphragm action of the slab is simulated by a linear equation constraint, imposing equal horizontal displacements to the nodes of the beams.

To capture the local buckling and the strength and stiffness deterioration due to cycling inelastic loading, the fuses and the end plates bolted on the fuses are modelled using C3D8R solid elements. Appropriate multi-point constraints are defined between the beam elements and the fuse end plates to allow for the correct transition of stresses. To evaluate the accuracy of this more simplified model, a beam-column sub-model is constructed and calibrated against the results by Shen et al. [17]. Fig. 10a shows the beam-solid sub-model and Fig. 10b illustrates that it can still capture the experimental force-displacement hysteresis with acceptable accuracy by using the same material parameters adopted for the more detailed model of the beam fuse.

The SSD-WHPs and the friction pads are modelled using nonlinear connector elements. As shown in Fig. 11a, connectors are spring-like elements with an elastoplastic force-displacement law. An elastic perfectly plastic force-displacement law is defined for connectors modelling the friction pads. The cyclic hardening parameters of the connectors modelling the WHPs are calibrated based on tests and additional FEM analyses, as follows. First, the experimental force-displacement response of an SSD-WHP, given in [35], is used to define the response parameters of the connector element as ‘half-cycle’ data. This force-displacement law definition is convenient if the experimental data is available because it can capture the combined isotropic-kinematic hardening without executing iterative simulations. Fig. 11b shows the force-displacement comparison of a connector element with a tested SSD-WHP in [35] under the ANSI/AISC 341-10 loading protocol and indicates that connectors are

effective in modelling the cyclic response of the SSD-WHPs. The pinching behaviour at zero force observed in the tests is not captured due to the more simplified uniaxial nature of the connector element behaviour. Subsequently, for each different geometry of SSD-WHPs used on each storey of the prototype frame, a detailed solid element sub-model is constructed using a very fine mesh discretization, as shown in Fig. 12a. Each sub-model is subjected to the ANSI/AISC 341-10 cyclic loading protocol using the material hardening parameter calibration adopted in the detailed model. The resulting hysteretic response is extracted and used as input for a half-cycle in the force-displacement law definition of the corresponding connectors. A typical comparison between the detailed sub-model and a connector element is shown in Fig. 12b. Taking into account that three-dimensional effects cannot be captured by a connector element, the agreement is considered acceptable.

To compare the seismic performance of the proposed CBF-MRF with that of the BRBF-MRF, a simplified model of the dual BRBF-MRF is also constructed. The geometry is identical to the beam-solid model of the dual CBF-MRF, but the SSD-WHPs are removed and concentric BRBs are used to resist the lateral force. The BRBs are modelled as connector elements with elastoplastic behaviour, assigning a post-yield stiffness ratio of 0.01 based on component test results reported in [41].

5 NONLINEAR MONOTONIC AND CYCLIC STATIC ANALYSES

5.1 Nonlinear monotonic static analysis results

Nonlinear monotonic static (pushover) analyses on the dual CBF-MRF are performed using both the detailed model and the simplified model. A triangular pattern of the lateral forces based on the height-wise mass distribution is used for the pushover analyses. A comparison of the base shear (V) versus roof drift, i.e. the roof horizontal displacement over the height of the building denoted as θ_r, responses of the two models is shown in Fig. 13 and demonstrates a very good agreement between the two modelling techniques. However, the detailed model is used for the rest of the pushover analyses on the dual CBF-MRF because it incorporates the friction pads, providing more detailed information on the failure modes of the proposed system for drifts larger than 3%. Fig. 14 shows contour plots of the equivalent plastic strain on the deformed shapes of the WHP-gusset plate connection and the beam-column-fuse region at θ_r= 1.35% (i.e. the roof drift expected under the MCE) and θ_r= 3%. The results show that the beams, columns and braces are damage-free for roof drifts far beyond those expected

under the MCE, whereas the SSD-WHPs and beam fuses are the only elements that experience plastic deformations.

The base shear coefficient, i.e. V normalised by the seismic weight (W) of the building, versus the roof drift responses of the conventional BRBF-MRF and the dual CBF-MRF are compared in Fig. 15. The design base shear (V_{des}) over W is also indicated on the graph. The target FOE, DBE and MCE roof drifts are indicated on the graphs. The sequence of the failure modes of the two frames is also noted on the curves. For the proposed dual CBF-MRF, the failure modes and corresponding roof drift levels are: SSD-WHP yielding at θ_r= 0.25%; beam fuse yielding at θ_r= 0.4%; and column base yielding immediately above the base gusset plates at θ_r= 0.65%. For the conventional BRBF-MRF, the failure modes and corresponding roof drift levels are: BRB yielding at θ_r= 0.3%; beam fuse yielding at θ_r= 0.45%; and column base yielding at θ_r= 0.64%. The two systems have comparable initial stiffness and similar base shear strength at first yield. The BRBF-MRF shows softening due to yielding of the BRBs, whereas the dual CBF-MRF shows softening due to yielding of SSD-WHPs and the beam fuses. However, the proposed dual CBF-MRF shows significantly higher post-yield stiffness. This is entirely attributed to the increased post-yield stiffness of the SSD-WHPs. As a result of the high post-yield stiffness, the dual CBF-MRF exhibits a considerably higher over-strength ratio (or reserve strength, defined as the base shear at a given drift divided by the first yield base shear) than the BRBF-MRF. The over-strength ratios at the DBE level are 1.24 and 1.75 for the BRBF-MRF and the dual CBF-MRF, respectively. The corresponding values at the MCE level are 1.27 and 2.02.

SSD-WHP fracture is not modelled explicitly; however, the experiments conducted by Vasdravellis et al. [35] showed that WHPs can achieve a ratio of fracture displacement to yield displacement, i.e. cyclic ductility, at least equal to ten under the standard seismic loading protocols that follow the recommendations of ANSI-AISC 341-10 [37] and FEMA 461 [42]. This observation was consistent for all the three steel grades and two different geometries of WHPs tested in the same study, with the WHPs made of SSD material achieving a cyclic ductility of twelve. Fracture of SSD-WHPs is crucial for the proposed frame, since it may result in a sudden drop of strength, accelerating the collapse of the frame. However, to assess the SSD-WHP fracture in a braced configuration as used in the proposed system, more tests are needed in order to take into account the appropriate boundary conditions and the expected loading history in a braced frame. For this initial evaluation study, it is assumed that an SSD-WHP fractures when the cyclic ductility demand reaches a value of ten. Although this assumption is inconclusive, it provides a fairly reasonable

estimation on the likelihood of fracture of an SSD-WHP, until more experimental data allow for a more accurate simulation of WHP fracture. Therefore, to maximise the fracture capacity of SSD-WHPs, their geometry is designed in such a way that they provide the yield force required by the seismic design while they have yield displacement as large as possible. This can be easily realised, since the required yield force of a WHP can be achieved with different combinations of D_e, D_i and L_{WHP}, and, thus, the stiffness can be modified as required. For the present frame, the yield displacement of each SSD-WHP geometry used on each floor is given in Table 2; for example, the SSD-WHPs installed on floor 2 yield at 5.4 mm, so it is assumed that they will fracture once the imposed displacement is 54 mm. The fracture of SSD-WHPs defines another limit state for the dual CBF-MRF and is indicated in Fig. 15 as "1st WHP fracture", i.e. denoting when the displacement demand will exceed ten times the yield displacement for the first time in an SSD-WHP. The monotonic pushover curve shows that the first SSD-WHP will fracture at θ_r= 2.5%.

5.2 Nonlinear cyclic static analysis results

Fig. 16a shows the V/W-θ_r responses of the dual CBF-MRF and the conventional BRBF-MRF resulting from nonlinear cyclic (push-pull) static analyses. Displacement-controlled analyses are performed using a triangular force distribution. Both systems are subjected to three cycles up to the FOE, DBE and MCE target drifts.

Both frames show large energy dissipation capacity. Similarly to the monotonic pushover analyses results, the cyclic inelastic behaviour of the two systems is noticeably different: the proposed frame possesses a significantly higher post-yield stiffness than the conventional frame as a result of the SSD material used for the WHPs. In addition, the nonlinear cyclic static analyses curves show that the residual drifts of the proposed dual CBF-MRF are smaller than those of the BRBF-MRF. The nonlinear dynamic analyses, however, will provide a more realistic estimation of the expected seismic response and residual drifts of the two systems.

Fig. 16b shows the cyclic pushover curves of the dual CBF-MRF obtained from the detailed and the simplified FEM models. A good agreement is observed between the responses of the two models, with a slightly lower base shear strength showed by the simplified model. Therefore, the simplified FEM model can be reliably used for nonlinear dynamic analyses.

6 NONLINEAR DYNAMIC ANALYSES

Nonlinear dynamic analyses are conducted to evaluate the seismic performance of the dual CBF-MRF and the BRBF-MRF. A set of 22 ground motions selected from the FEMA P695 database [43] is used, as listed in Table 4. The ground motion records are scaled to the FOE, DBE and MCE seismic hazard levels, according to the procedure based on the recommendations of FEMA P695 [43]. The scale factors obtained from this procedure are also summarised in Table 4. Spectra of the record set are scaled to match the spectral acceleration for the given hazard level at the fundamental period of the structure, which is computed using eigenvalue analysis. None of the records presents near-fault forward directivity effects.

6.1 Modelling for nonlinear dynamic analysis

The time history analyses are performed using the simplified FEM models of the proposed dual CBF-MRF and the conventional BRBF-MRF. To correctly take into account the seismic masses of the frame, the two external bays of the perimeter frame (see Fig. 3) are also included in the model along with the corresponding gravity loads. The mass is calculated on the basis of the dead plus one-third live load combination. Additional lumped masses are assigned to the beam elements to account for the total tributary mass to the perimeter frame. Beam elements with pinned beam-column and column-base connections are used to define the additional bays. The dynamic analyses are performed using the implicit dynamic algorithm of Abaqus [34]. The Hilber-Hughes-Taylor method is used by default to integrate the dynamic equations along with a Newton-like method to trace the nonlinear solution within a time step. The maximum time step is set ten times smaller than the input time step of the accelerogram to allow for an accurate estimation of the nonlinear response. Rayleigh damping equal to three percent of the critical damping is assigned to the first and second modes of the structures, following the approach recommended in [44]. A nonlinear load-controlled static analysis under gravity loads is first performed, and then the nonlinear dynamic time history analysis for each ground motion is executed. Each dynamic analysis is extended well beyond the actual earthquake time to allow for damped free vibration decay and accurate calculation of the residual drifts.

6.2 Nonlinear dynamic analysis results

Fig. 17 shows θ_r time histories of the dual CBF-MRF and BRB-MRF under the no. 16 record scaled to the DBE and MCE ground motions. Comparison of the response time histories

reveals a significant difference in the residual drift values between the two systems. It is seen that, after the end of the ground motion, the BRBF-MRF oscillates and finds static equilibrium with appreciable residual drifts, whereas the dual CBF-MRF has a clear tendency to re-centre. Under the DBE ground motion, both systems experience a $\theta_{s,max}$ approximately equal to 1%. At the end of the imposed time history, the BRBF-MRF has a maximum residual drift ($\theta_{s,res,max}$) equal to 0.4%, whereas the proposed CBF-MRF has a negligible $\theta_{s,res,max}$= 0.09%. Under the MCE ground motion, the BRBF has $\theta_{s,max}$= 1.88% and $\theta_{s,res,max}$= 1.07%. The corresponding values of the dual CBF-MRF are 1.56% and 0.38%. It is concluded that, under this particular accelerogram, even though the two systems experience similar peak storey drifts, the higher post-yield stiffness of the proposed frame results in a drastic reduction of residual drifts, avoiding repair and disruption even after that very severe MCE record.

Fig. 18 shows the statistics of the storey drifts (θ_s) and residual drifts ($\theta_{s,res}$) throughout the height of the dual CBF-MRF under the FOE, DBE and MCE records, in terms of mean (m), median, and mean plus standard deviation ($m+\sigma$) values. Similar statistics are shown in Fig. 19 for the BRBF-MRF under the DBE and MCE records. The $\theta_{s,max}$ and $\theta_{s,res,max}$ values typically occur in the third storey for the dual CBF-MRF and in the sixth storey for the BRBF-MRF. Comparison of the graphs in Figs. 18 and 19 reveals that, while the storey drift profiles of the two frames are comparable and close to the target design values, the residual drifts of the proposed frame are significantly reduced. In particular, the residual drifts experienced by the dual CBF-MRF have values that are negligible under the FOE, very low under the DBE and well below the assumed reparability limit of 0.5% under the MCE records. In addition, even under the most severe MCE ground motions, the friction pads in the CBF-MRF are not activated, having no impact on the drift behaviour. The BRBF-MRF has significantly greater residual storey drifts than the dual CBF-MRF under the DBE and MCE earthquake records. In addition, it is observed that the standard deviation of the residual drifts is much smaller in the dual CBF-MRF system, with the $m+\sigma$ under the MCE being still well below 0.5%. The higher standard deviation of the residual drifts of the BRBF-MRF implies that the system can experience residual drifts greater than the 0.5% limit, as shown in Fig. 19, with $m+\sigma$ reaching 0.80% under the MCE records.

Table 5 provides a summary of the statistics of $\theta_{s,max}$ and $\theta_{s,res,max}$ values for the two systems. The proposed dual frame has mean $\theta_{s,max}$ equal to 0.47% under the FOE, 0.88% under the DBE and 1.27% under the MCE. These values are slightly lower than the design target values (i.e. 0.48%, 0.96%, and 1.44%). The BRBF-MRF has slightly greater mean

$\theta_{s,max}$ than the CBF-MRF, i.e. 1.02% and 1.52% under the DBE and MCE, respectively. The mean $\theta_{s,res,max}$ for the dual CBR-MRF is 0.02% under the FOE, 0.06% under the DBE and 0.12% under the MCE. The BRBF-MRF exhibited nearly five times larger mean $\theta_{s,res,max}$ under the DBE (0.27%) and almost four times larger mean $\theta_{s,res,max}$ under the MCE (0.44%). The $m+\sigma$ of $\theta_{s,res,max}$ for the dual CBF-MRF are 0.10% and 0.23% under the DBE and MCE, respectively, i.e. still very low. The corresponding values for the BRBF-MRF are 0.49% and 0.80%, demonstrating a much higher scatter in the results. Therefore, the dynamic analyses results show that the proposed dual CBF-MRF is able to drastically reduce the residual drifts and, thus, enable repair without significant disruption to the building use or occupation even after a very rare MCE seismic event.

The results of this study are compared to the results of previous research studies concerning experimental or numerical nonlinear dynamic analyses on prototype BRBFs [6, 8, 9, 10, 11, 12]. Table 6 shows the results of those studies in terms of mean $\theta_{s,res,max}$ under FOE, DBE and MCE records, where applicable. Apart from the prototype BRBFs tested in [9] and [10], all other prototypes have six stories and comparable fundamental period to the prototype frame used in this study, i.e. 0.77 s. The results of the previous studies show that BRBFs can exhibit mean $\theta_{s,res,max}$ in the range of 0.3-1.3% and 1.2-3.9% under DBE and MCE ground motions, respectively. Although the scatter in residual drifts is quite large, these values suggest that significant permanent deformations may occur in BRBFs under strong seismic excitations, resulting in non-reparable damage. In the study conducted by Kiggins and Uang [12] on a 6-storey building with BRBs, $\theta_{s,res,max}$ were reduced by using a backup MRF, i.e. from 0.29% to 0.13% under the DBE. However, it is seen from Table 6 that the proposed dual CBF-MRF achieves an even more drastic reduction of residual drifts, i.e. from 0.27% in the BRBF-MRF to 0.06% (see Table 5).

Fig. 20 shows the statistics of the maximum displacement demands on the SSD-WHPs under the FOE, DBE, and MCE ground motion records in each storey. The yield displacement (u_y) of the SSD-WHPs of each story and the assumed fracture limit ($10u_y$) are also shown. The mean values of maximum displacement demand under the FOE and DBE are 8.4 mm and 17 mm, respectively. For the MCE hazard level, SSD-WHPs reach displacements with a mean value equal to 23 mm in the third storey. These results suggest that the displacement demands imposed on the SSD-WHPs are well below the assumed fracture value of ten times the yield displacement; therefore, there is a very small likelihood of fracture for seismic events up to MCE.

Fig. 21 shows the deformed shape of the connection with the beam fuse under no. 16 record scaled to MCE. Equivalent plastic strain contours obtained from the analysis are illustrated for the peak imposed deformation. The results clearly indicate that plastic deformations (damage) are concentrated only in the beam fuse, thus preserving the integrity of the other main structural components.

7 CONCLUSIONS

In this work, a dual seismic-resistant system (denoted as CBF-MRF) consisting of a steel moment-resisting frame equipped with high post-yield stiffness braces and replaceable beam fuses was presented and numerically evaluated. The high post-yield stiffness is achieved by using duplex stainless steel pins (denoted as SSD-WHPs) in series with the braces. The seismic performance of the CBF-MRF was evaluated by means of advanced numerical simulations using models of different complexity. Based on the results presented herein, the following conclusions are drawn:

- A simplified model of the CBF-MRF using beam elements for the main structural members, nonlinear connector elements for the SSD-WHPs and solid elements for the beam fuses, is found to provide a similar level of accuracy with a detailed FEM model using shell and solid elements.

- Nonlinear static monotonic and cyclic analyses performed using the detailed FEM model show that the proposed design methodology and capacity design rules guarantee that inelastic deformations are concentrated only in the SSD-WHPs and beam fuses, whereas the main structural components are essentially elastic even for drifts expected under the maximum considered earthquake (MCE).

- The proposed frame can be designed to have stiffness and strength comparable with a conventional buckling-restrained braced moment frame (BRBF-MRF), but exhibits a much higher post-yield stiffness owing to the properties of the duplex stainless steel material used for the SSD-WHPs. The proposed system achieves an over-strength ratio higher than 2 under the MCE.

- Nonlinear dynamic analyses performed using the simplified FEM model show that the proposed CBF-MRF and the conventional BRBF-MRF experience comparable peak storey drifts. However, the combined effects of the high post-yield stiffness and the appreciable elastic displacement capacity of the MRF drastically reduce the maximum residual drift of the dual CBF-MRF. The maximum residual drift of the proposed frame is negligible under the

FOE, has a mean value of 0.06% under the design basis earthquake (DBE) and a mean value of 0.12% under the very rare MCE. The maximum residual drift experienced by the BRBF-MRF is five times larger under the DBE and nearly four times larger under the MCE.

- The SSD-WHPs are designed in such a way that they have a large yield displacement, and therefore, a reduced likelihood of fracture based on observations from previous tests. However, further experiments need to be carried out on the fracture capacity of SSD-WHPs installed in brace members in order to reliably account for their fracture capacity and its effect on the collapse capacity of the proposed frame.

It is noted that the effectiveness of the proposed system should be evaluated by considering more building typologies, i.e. including different building heights and number or span length of bays.

REFERENCES

[1] CEN. Eurocode 8: design provisions for earthquake resistance of structures - part 1: general rules, seismic actions and rules for building. Brussels: European Committee for Standardization; 2004.

[2] Iwata Y, Sugimoto H, Kuguamura H. Reparability limit of steel structural buildings based on the actual data of the Hyogoken-Nanbu earthquake. 38th Joint Panel on Wind and Seismic Effects: NIST Special Publication 1057; 2006. p. 23-32.

[3] McCormick J, Aburano H, Ikenaga M, Nakashima M. Permissible residual deformation levels for building structures considering both safety and human elements. 14th World Conference on Earthquake Engineering, Beijing, China; 2008.

[4] Watanabe A, Hitomi Y, Saeki E, Wada A, Fujimoto M. Properties of brace encased in buckling-restraining concrete and steel tube. 9th World Conference on Earthquake Engineering, Tokyo-Kyoto, Japan; 1988.

[5] Iwata M, Kato T, Wada A. Buckling-restrained braces as hysteretic dampers. 3rd International Conference STESSA, Montreal, Canada; 2000.

[6] Sabelli R, Mahin S, Chang C. Seismic demands on steel braced frame buildings with buckling-restrained braces. Eng Struct 2003;25:655-66.

[7] ASCE. Minimum design loads for buildings and other structures. ASCE/SEI 7-10. Reston, VA: American Society of Civil Engineers; 2010.

[8] Erochko J, Christopoulos C, Tremblay R, Choi H. Residual drift response of SMRFs and BRB frames in steel buildings designed according to ASCE 7-05. J Struct Eng 2011;137(5):589-99.

[9] Fahnestock LA, Sause R, Ricles JM. Seismic response and performance of buckling-restrained braced frames. J Struct Eng 2007;133(9):1195-1204.

[10] Fahnestock LA, Ricles JM, Sause R. Experimental evaluation of a large-scale buckling-restrained braced frame. J Struct Eng 2007;133(9):1205-14.

[11] Sahoo DR, Chao S. Stiffness-based design for mitigation of residual displacements of buckling-restrained braced frames. J Struct Eng 2015;141(9):04014229.

[12] Kiggins S, Uang CM. Reducing residual drift of buckling-restrained braced frames as a dual system. Eng Struct 2006;28(11):1525-32.

[13] Balut N, Gioncu V. Suggestion for an improved 'dog-bone' solution. 4th International Conference STESSA, Naples, Italy; 2003.

[14] Bruneau M, Uang CM, Sabelli R. Ductile design of steel structures. New York, NY: McGraw-Hill; 2011.

[15] Vayas I, Thanopoulos P. Innovative dissipative (INERD) pin connections for seismic resistant braced frames. Int J Steel Struct 2005;5(5):453-464.

[16] Gray M, Christopoulos C, Packer J. Cast steel yielding brace system for concentrically braced frames: concept development and experimental validations. J Struct Eng 2014;140(4):04013095.

[17] Shen Y, Christopoulos N, Mansour C, Tremblay R. Seismic design and performance of steel moment-resisting frames with nonlinear replaceable links. J Struct Eng 2011;137(10):1107-17.

[18] Mansour N, Christopoulos C, Tremblay R. Experimental validation of replaceable shear links for eccentrically braced steel frames. J Struct Eng 2011;137(10):1141-52.

[19] Castiglioni CA, Kanyilmaz A, Calado L. Experimental analysis of seismic resistant composite steel frames with dissipative devices. J Constr Steel Res 2012;76:1-12.

[20] Ricles J, Sause R, Garlock M, Zhao C. Posttensioned seismic-resistant connections for steel frames. J Struct Eng 2001;127(2):113-21.

[21] Ricles J, Sause R, Peng SW, Lu LW. Experimental evaluation of earthquake resistant posttensioned steel connections. J Struct Eng 2002;128(7):850-59.

[22] Garlock M, Ricles JM, Sause R. Experimental studies of full-scale posttensioned steel connections. J Struct Eng 2005;131(3):438-48.

[23] Christopoulos C, Filiatrault A, Uang CM, Folz B. Posttensioned energy dissipating connections for moment-resisting steel frames. J Struct Eng 2002;128(9):1111-20.

[24] Chou CC, Chen JH, Chen YC, Tsai KC. Evaluating performance of post-tensioned steel connections with strands and reduced flange plates. Earthq Eng Struct Dyn 2006;35(9):1167-85.

[25] Vasdravellis G, Karavasilis TL, Uy B. Large-scale experimental validation of steel posttensioned connections with web hourglass pins. J Struct Eng 2013;139(6):1033-42.

[26] Rojas P, Ricles JM, Sause R. Seismic performance of post-tensioned steel moment resisting frames with friction devices. J Struct Eng 2004;131(4):529-40.

[27] Kim HJ, Christopoulos C. Friction damped posttensioned self-centering steel moment-resisting frames. J Struct Eng 2008;134(11):1768-79.

[28] Tsai KC, Chou CC, Lin CL, Chen PC, Jhang SJ. Seismic self-centering steel beam-to-column moment connections using bolted friction devices. Earthq Eng Struct Dyn 2008;37:627-45.

[29] Wolski M, Ricles JM, Sause R. Experimental study of a self-centering beam-column connection with bottom flange friction device. J Struct Eng 2009;135(5):479-88.

[30] Christopoulos C, Tremblay R, Kim HJ, Lacerte M. The self-centering energy dissipative (SCED) bracing system for the seismic resistance of structures: development and validation. J Struct Eng 2008;134(1):96-107.

[31] Miller DJ, Fahnestock LA, Eatherton MR. Development and experimental validation of a nickel–titanium shape memory alloy self-centering buckling-restrained brace. Eng Struct 2012;40:288-298.

[32] Pettinga D, Christopoulos C, Pampanin S, Priestley N. Effectiveness of simple approaches in mitigating residual deformations in buildings. Earthq Eng Struct Dyn 2008;36(12);1763-83.

[33] CEN. Eurocode 3: design of steel structures - part 1-1: general rules and rules for building. Brussels: European Commitee for Standardization; 2003.

[34] Hibbit D, Karlsson B, Sorensen P. ABAQUS/Standard analysis user's manual, version 6.13. Providence, RI: Dassault Systèmes/Simulia; 2013.

[35] Vasdravellis G, Karavasilis TL, and Uy B. Design rules, experimental evaluation, and fracture models for high-strength and stainless steel hourglass shape energy dissipation devices. J Struct Eng 2014;140(11):04014087.

[36] CEN. Eurocode 1: actions on structures - part 1-4: general actions – wind actions. Brussels: European Commitee for Standardization; 2004.

[37] AISC. Seismic provisions for structural steel buildings. ANSI/AISC 341-10. Chicago, IL: American Institute of Steel Construction; 2010.

[38] AISC. Prequalified connections for special and intermediate steel moment frames for seismic applications. ANSI/AISC 358-10. Chicago, IL: American Institute of Steel Construction; 2010.

[39] Thornton WA. Bracing connections for heavy construction. AISC Eng J 1984;21(3):139-48.

[40] Vasdravellis G, Karavasilis TL, Uy B. Finite element models and cyclic behavior of self-centering steel post-tensioned connections with web hourglass pins. Eng Struct 2013; 52:1-16.

[41] Ariyaratana C, Fahnestock LA. Evaluation of buckling-restrained braced frame seismic performance considering reserve strength. Eng Struct 2011;33(1):77-89.

[42] FEMA 461. Interim testing protocols for determining the seismic performance characteristics of structural and non-structural components. CA: Applied Technology Council; 2007.

[43] FEMA P695. Quantification of building seismic performance factors. ATC-63 Project. CA: Applied Technology Council; 2008.

[44] Zareian F, Medina A. A practical method for proper modelling of structural damping in inelastic plane structural systems. Comput Struct 2010;88(1):45-53.

Table 1. Design details of the conventional BRBF-MRF.

Storey	Column	Beam	BRB core cross-section area (mm^2)	$F_{y,BRB}$ (kN)	K_{BRB} (N/mm)
6	HEB400	IPE330	500	150	30,000
5	HEB400	IPE330	1100	330	59,000
4	HEB400	IPE330	1530	460	80,000
3	HEB400	IPE330	1900	570	100,000
2	HEB500	IPE330	1950	585	108,000
1	HEB500	IPE330	1950	585	108,000

Table 2. Design details of the dual CBF-MRF.

Storey	Column	Beam	Brace	n_{WHP}	D_e (mm)	D_i (mm)	L_{WHP} (mm)	$F_{y,tot}$ (kN)	K_{tot} (N/mm)	u_y (mm)
6	HEB400	IPE330	HEA300	4	36	18	210	200	42,000	4.8
5	HEB400	IPE330	HEA300	4	42	24	230	330	59,000	5.6
4	HEB400	IPE330	HEA300	4	50	24	230	460	80,000	5.6
3	HEB400	IPE330	HEA300	4	50	24	225	450	80,000	5.6
2	HEB500	IPE330	HEA300	6	46	22	215	585	108,000	5.4
1	HEB500	IPE330	HEA300	6	46	22	215	585	108,000	5.4

Table 3. Design details of the beam fuse.

	Section	b_{beam} (mm)	d_{fuse} (mm)	l_{fuse} (mm)	M_{pl} (kNm)	$M_{max,col}$ (kNm)	$M_{pl,fuse}/M_{pl,beam}$
Fuse	IPE270	-	270	200	145	-	0.6
Beam	IPE330	160	-	42	241	198	-

Table 4. Ground motion records.

No.	Earthquake	Year	Recording station	Magnitude	Scaling factors		
					FOE	DBE	MCE
1	Northridge, USA	1994	Beverly Hills	6.7	0.36	0.72	1.08
2	Northridge, USA	1994	Canyon Country	6.7	0.52	1.05	1.58
3	Duzce, Turkey	1999	Bolu	7.1	0.35	0.71	1.06
4	Hector Mine, USA	1999	Hector	7.1	0.96	1.92	2.88
5	Imperial Valley, USA	1979	Delta	6.5	0.61	1.21	1.82
6	Imperial Valley, USA	1979	El Centro Array #11	6.5	0.86	1.72	2.57
7	Kobe, Japan	1995	Nishi-Akashi	6.9	0.45	0.91	1.36
8	Kobe, Japan	1995	Shin-Osaka	6.9	0.58	1.17	1.76
9	Kocaeli, Turkey	1999	Duzce	7.5	0.66	1.33	2.00
10	Kocaeli, Turkey	1999	Arcelik	7.5	1.96	3.89	5.83
11	Landers, USA	1992	Yermo Fire Station	7.3	0.69	1.38	2.07
12	Landers, USA	1992	Coolwater	7.3	0.91	1.81	2.72
13	Loma Prieta, USA	1989	Capitola	6.9	0.39	0.78	1.17
14	Loma Prieta, USA	1989	Gilroy Array #3	6.9	0.69	1.24	1.86
15	Manjil, Iran	1990	Abbar	7.4	0.48	0.97	1.46
16	Superstition Hills, USA	1987	El Centro Imp. Co.	6.5	0.51	1.02	1.53
17	Superstition Hills, USA	1987	Poe Road	6.5	0.85	1.69	2.54
18	Cape Mendocino, USA	1992	Rio Dell Overpass	7.0	0.54	1.08	1.63
19	Chi-Chi, Taiwan	1999	CHY101	7.6	0.50	1.00	1.50
20	Chi-Chi, Taiwan	1999	TCU045	7.6	0.66	1.33	1.99
21	San Fernando, USA	1971	LA - Hollywood Stor	6.6	1.61	3.23	4.85
22	Friuli, Italy	1976	Tolmezzo	6.5	0.82	1.65	2.47

Table 5. Storey drift summary.

Dual frame type	$\theta_{s,max}$ (%)	$\theta_{s,res,max}$ (%)

		m	$m+\sigma$	Median	m	$m+\sigma$	Median
CBF-MRF	FOE	0.47	0.56	0.49	0.02	0.04	0.01
	DBE	0.88	1.11	0.88	0.06	0.10	0.05
	MCE	1.27	1.62	1.19	0.12	0.23	0.10
BRBF-MRF	DBE	1.02	1.38	0.96	0.27	0.49	0.23
	MCE	1.52	2.06	1.38	0.44	0.80	0.37

Table 6. BRBF nonlinear dynamic analysis results from previous studies.

Reference	Frame type	Stories	T (s)	Mean $\theta_{s,res,max}$ (%)

				FOE	DBE	MCE
Sabelli et al. (2003) [6]	BRBF	6	0.90	0.40	0.70	2.20
Kiggins and Uang (2006) [12]	BRBF	6	0.77	-	0.29	-
	BRBF-MRF	6	0.77	-	0.13	-
Fahnestock et al. (2007) [9]	BRBF	4	-	-	0.50	1.20
Fahnestock et al. (2007) [10]	BRBF	4	0.71	0.20	1.30	2.70
Erochko et al. (2011) [8]	BRBF	6	1.05	-	1.30	3.90
Sahoo and Chao (2014) [11]	BRBF	6	0.97	-	0.41	-
This study	CBF-MRF	6	0.77	0.02	0.06	0.12

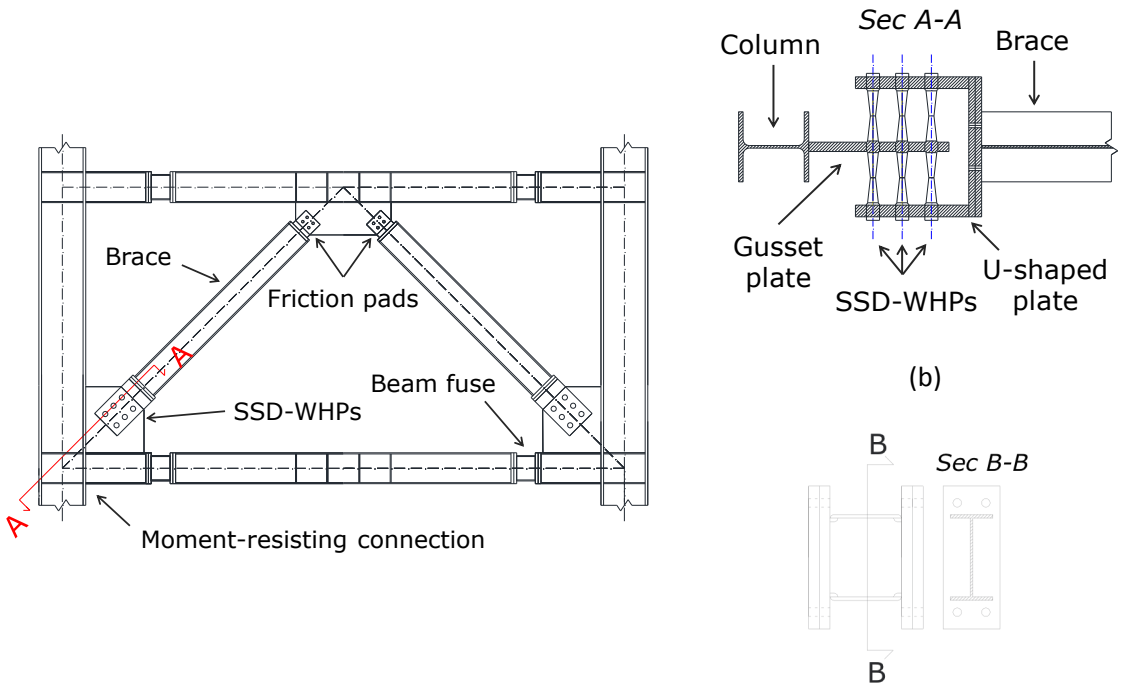

Fig. 1. Geometry of the proposed dual CBF-MRF: a) overview; b) brace-WHP connection detail; and c) beam fuse detail.

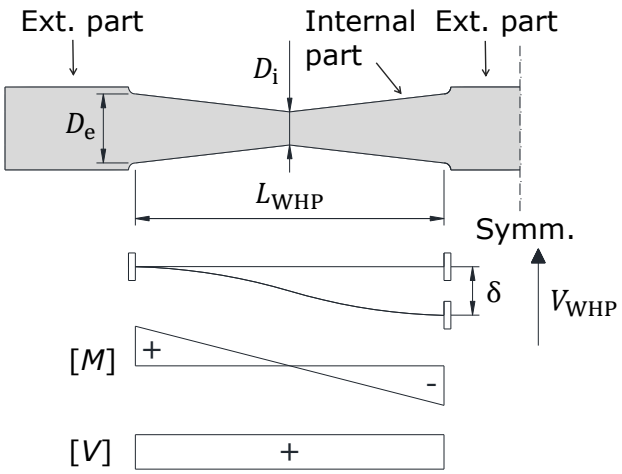

(a)

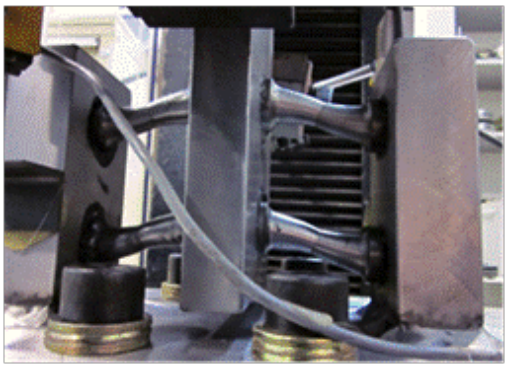

(b)

Fig. 2. Web-hourglass shape steel pin (WHP): (a) geometry, deflection, elastic bending moment and shear diagram; and (b) component test [25].

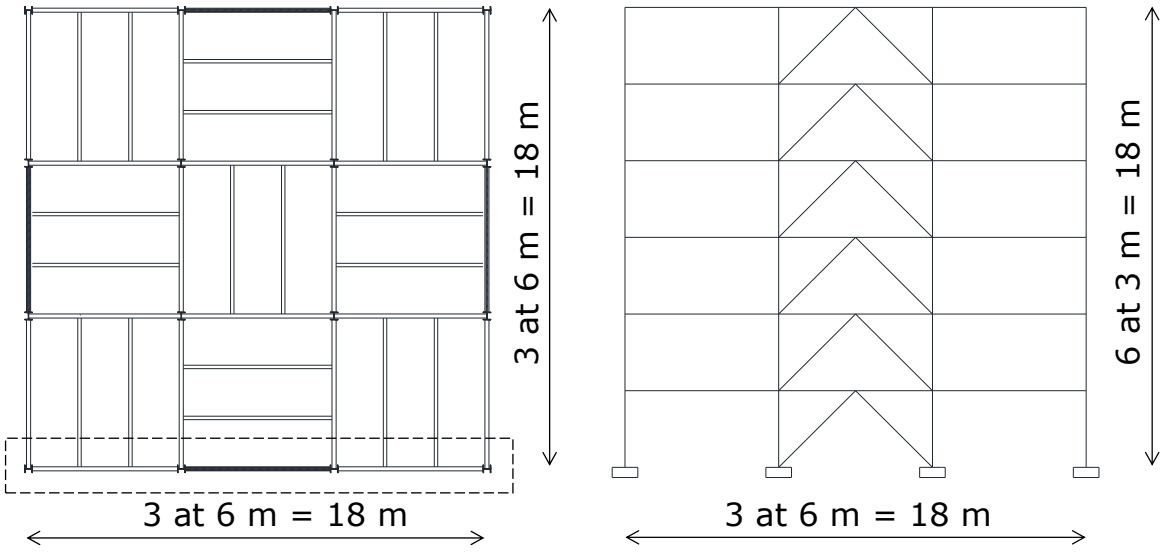

Fig. 3. Prototype building: (a) plan view; and (b) elevation of a perimeter frame.

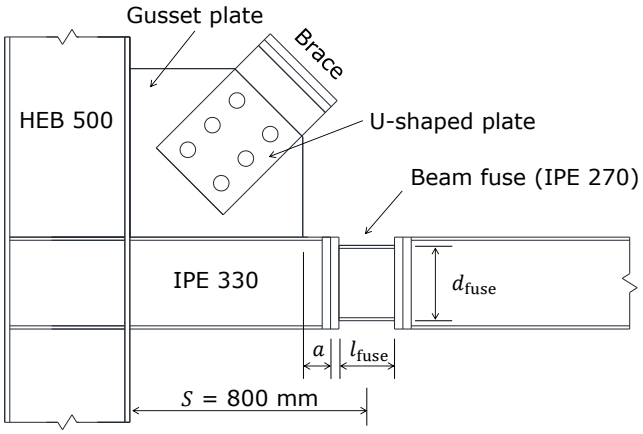

Fig. 4. Beam-column connection with the beam fuse.

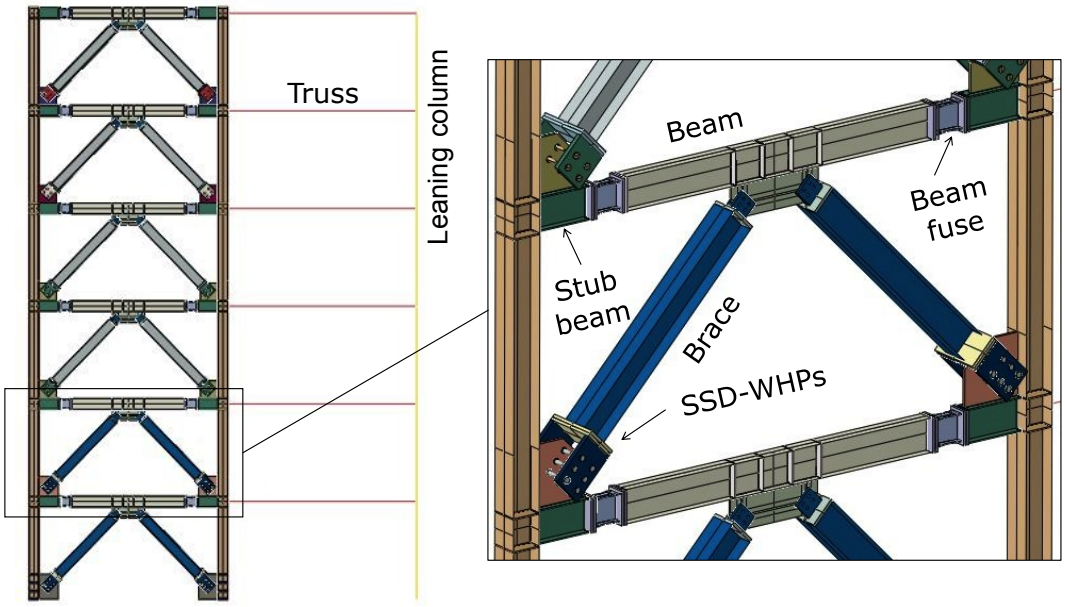

Fig. 5. View of the detailed solid-shell FEM model.

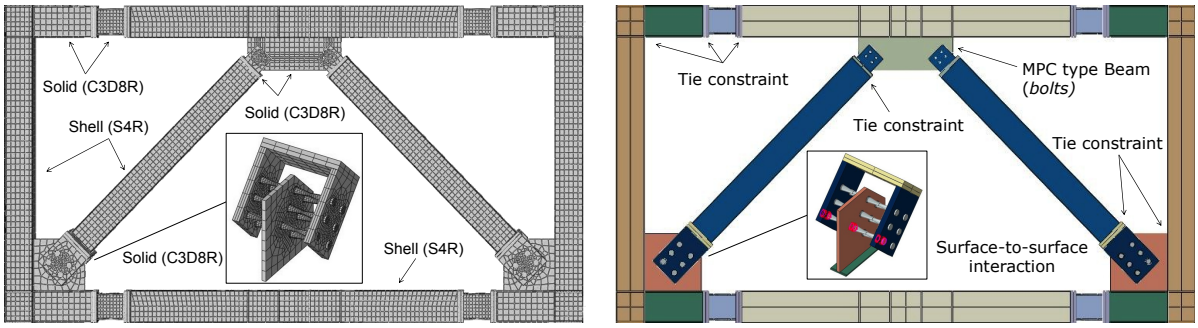

(a) (b)

Fig. 6. a) Mesh discretization; and b) interaction and constraint definitions of the detailed solid-shell FEM model.

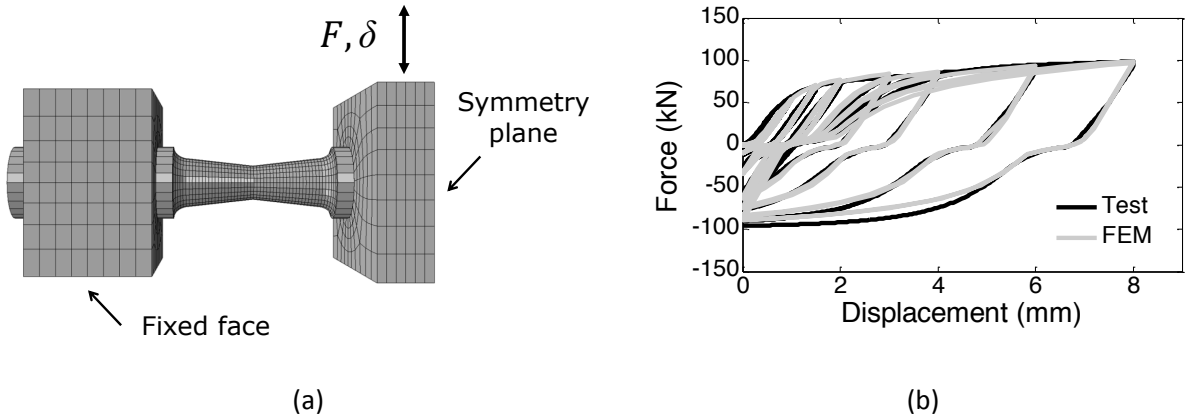

Fig. 7. a) FEM model of half of a WHP; and b) experimental and numerical hysteresis under the ANSI/AISC 341-10 loading protocol.

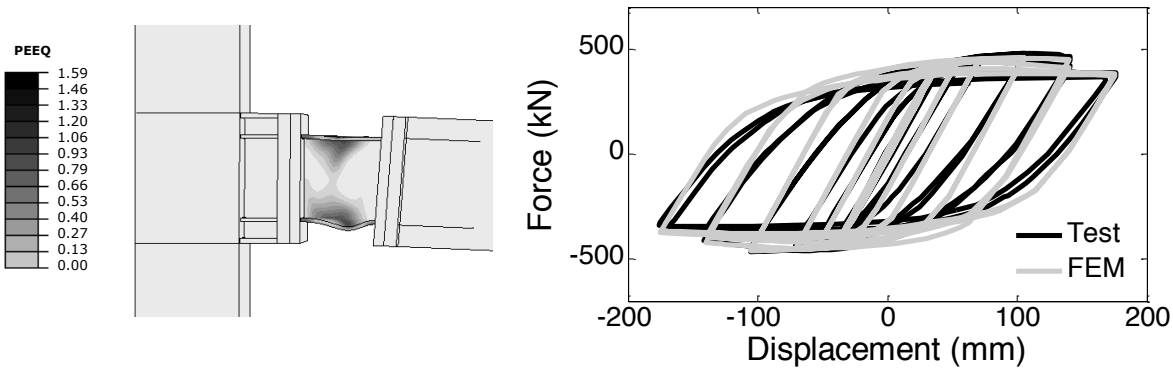

(a) (b)

Fig. 8. (a) Local flange and web buckling in the replaceable link (deformed shape and PEEQ distribution at 175 mm beam tip displacement); and (b) numerical results compared against the experimental behaviour of the replaceable link [17].

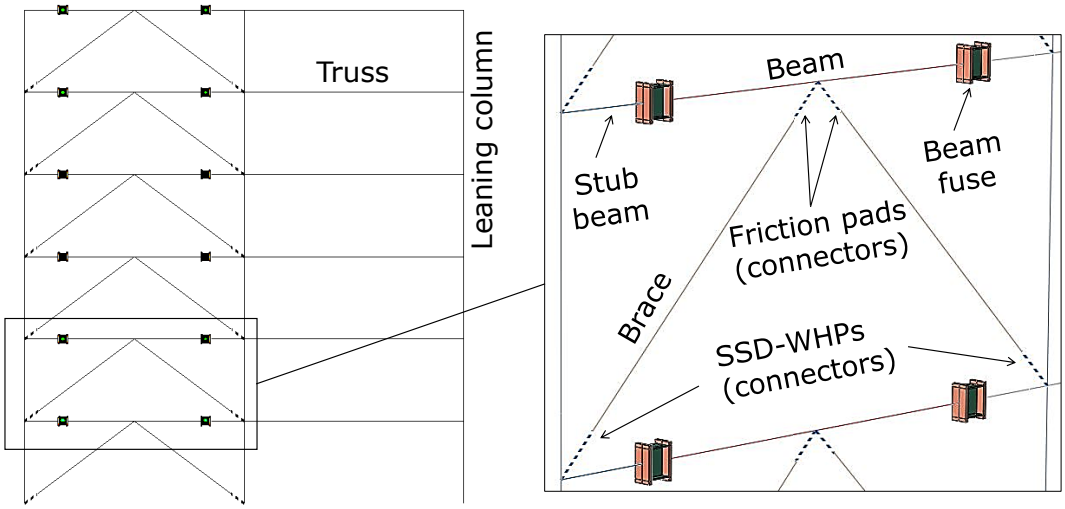

Fig. 9. View of the simplified beam-solid FEM model.

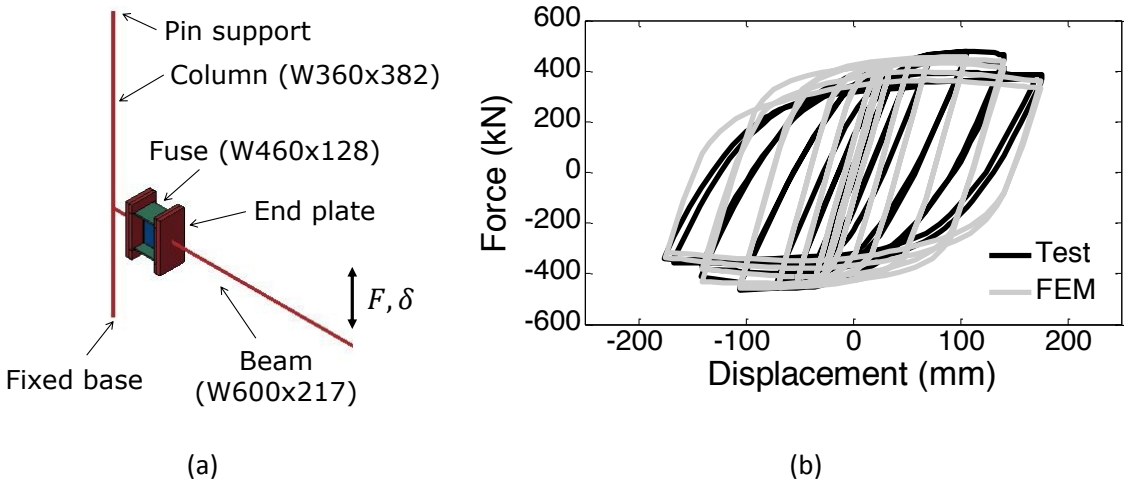

Fig. 10. (a) View of the beam-solid FEM sub-model for the beam-column connection with the beam fuse; (b) experimental [17] – numerical comparison of the force-displacement response.

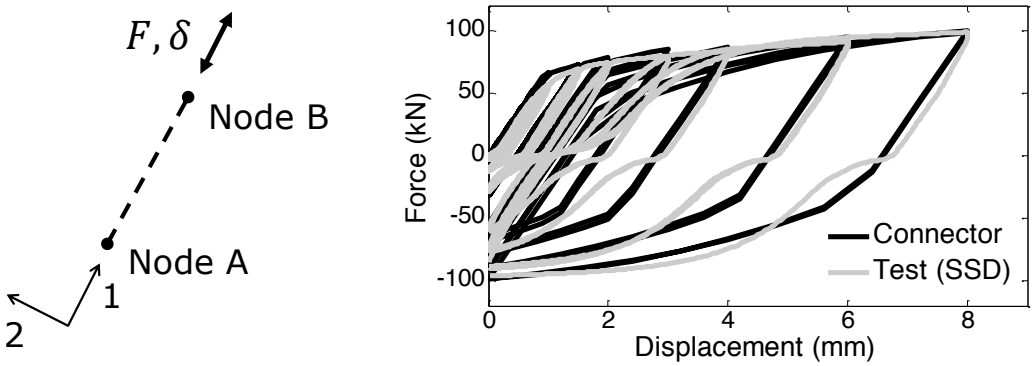

(a) (b)

Fig. 11. (a) Connector model definition; and (b) experimental [25] – connector model comparison of SSD-WHP response under the ANSI/AISC 341-10 loading protocol.

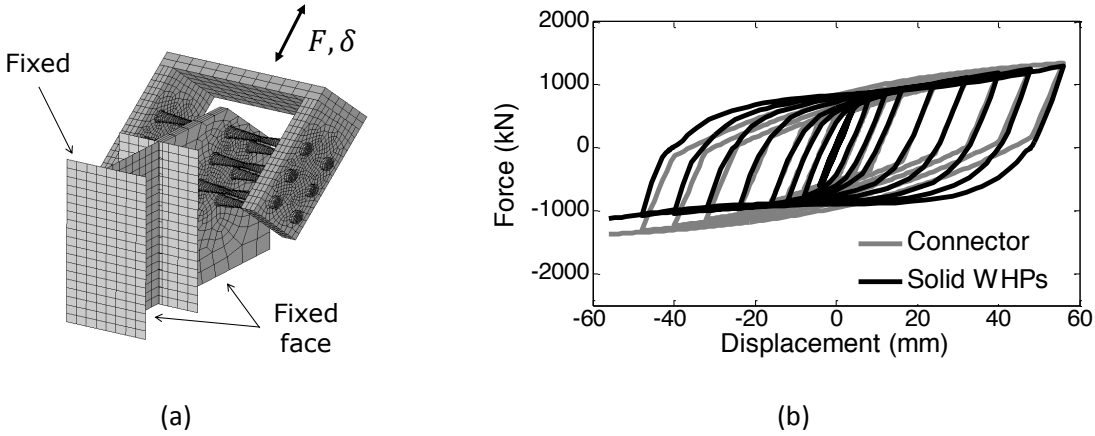

Fig. 12. (a) FEM sub-model of an isolated WHP-gusset plate connection; and (b) connector - FEM sub-model response comparison.

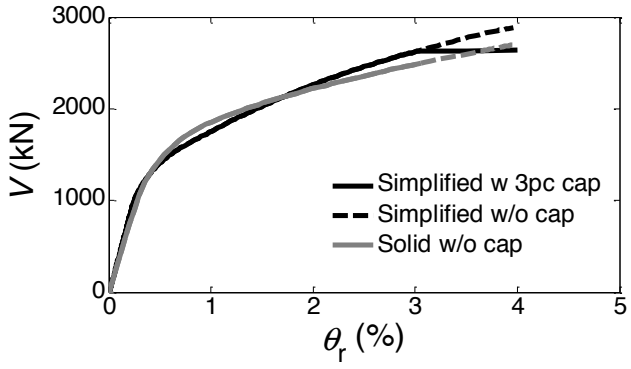

Fig. 13. Base shear-roof drift behaviour from nonlinear monotonic (pushover) static analysis.

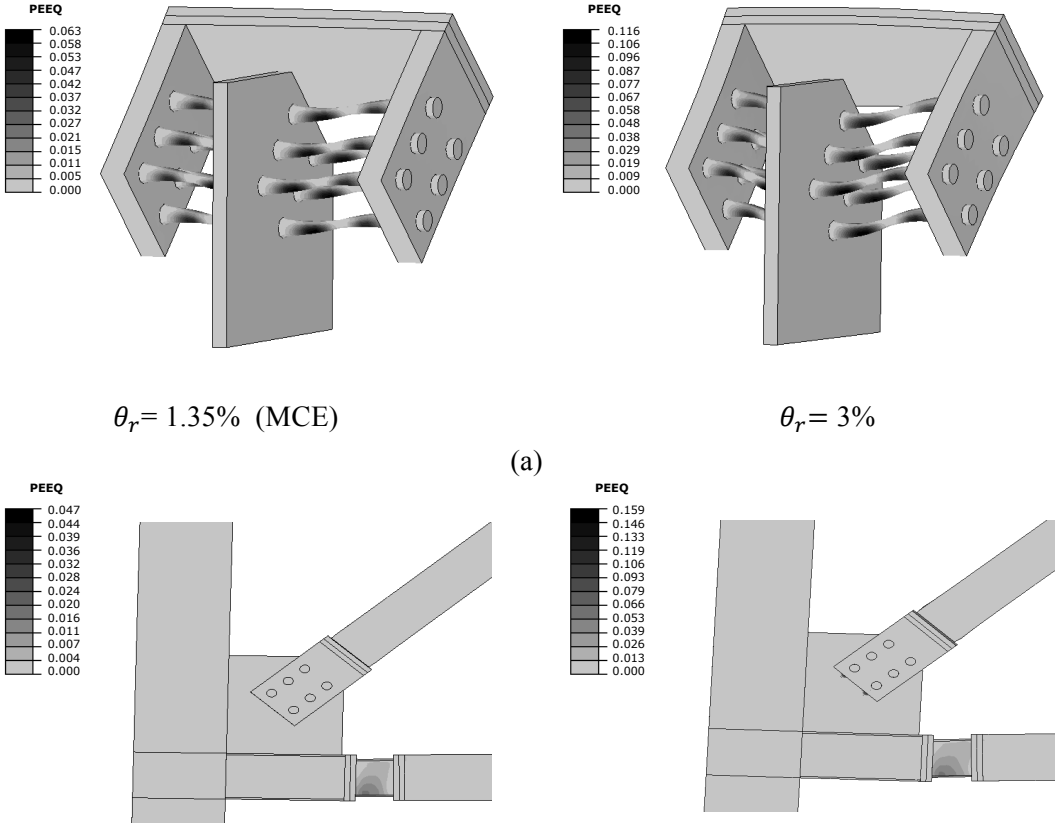

Fig. 14. Equivalent plastic strain (PEEQ) distribution: (a) connection with SSD-WHPs; and (b) beam-column connection with the beam fuse.

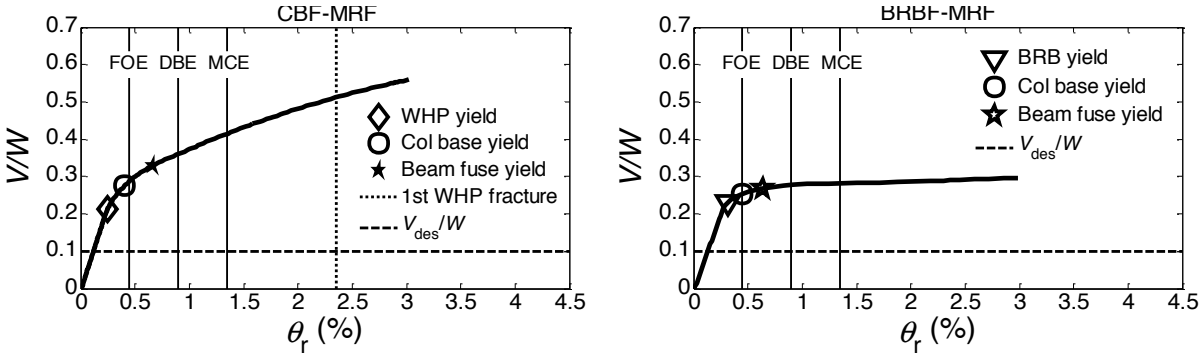

Fig. 15. Base shear-roof drift behaviour from nonlinear monotonic (pushover) static analysis.

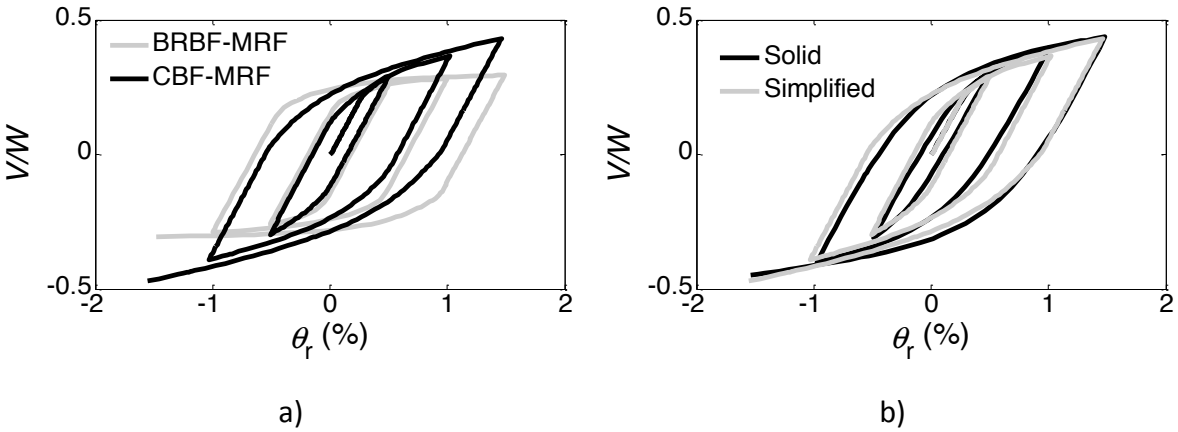

Fig. 16. Cyclic pushover response: a) dual CBF-MRF and conventional BRBF-MRF; and b) detailed and simplified FEM models.

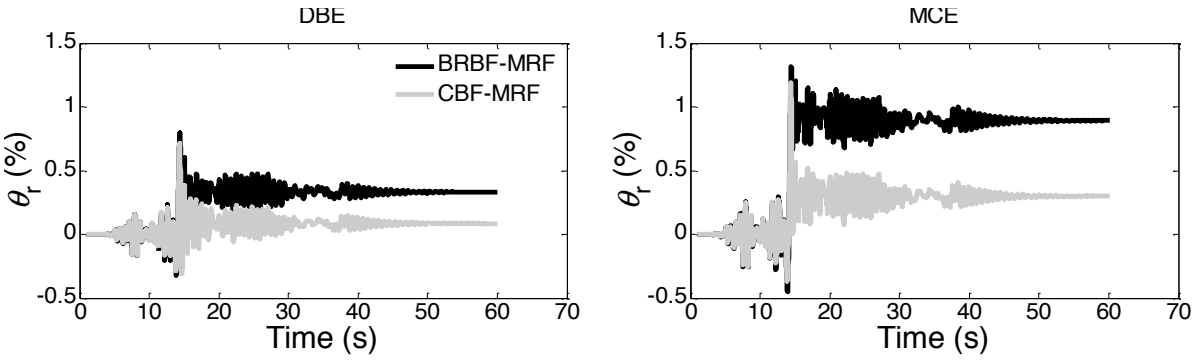

Fig. 17. Roof drift time histories under n.16 ground motion scaled to the DBE and MCE sesimic hazard levels.

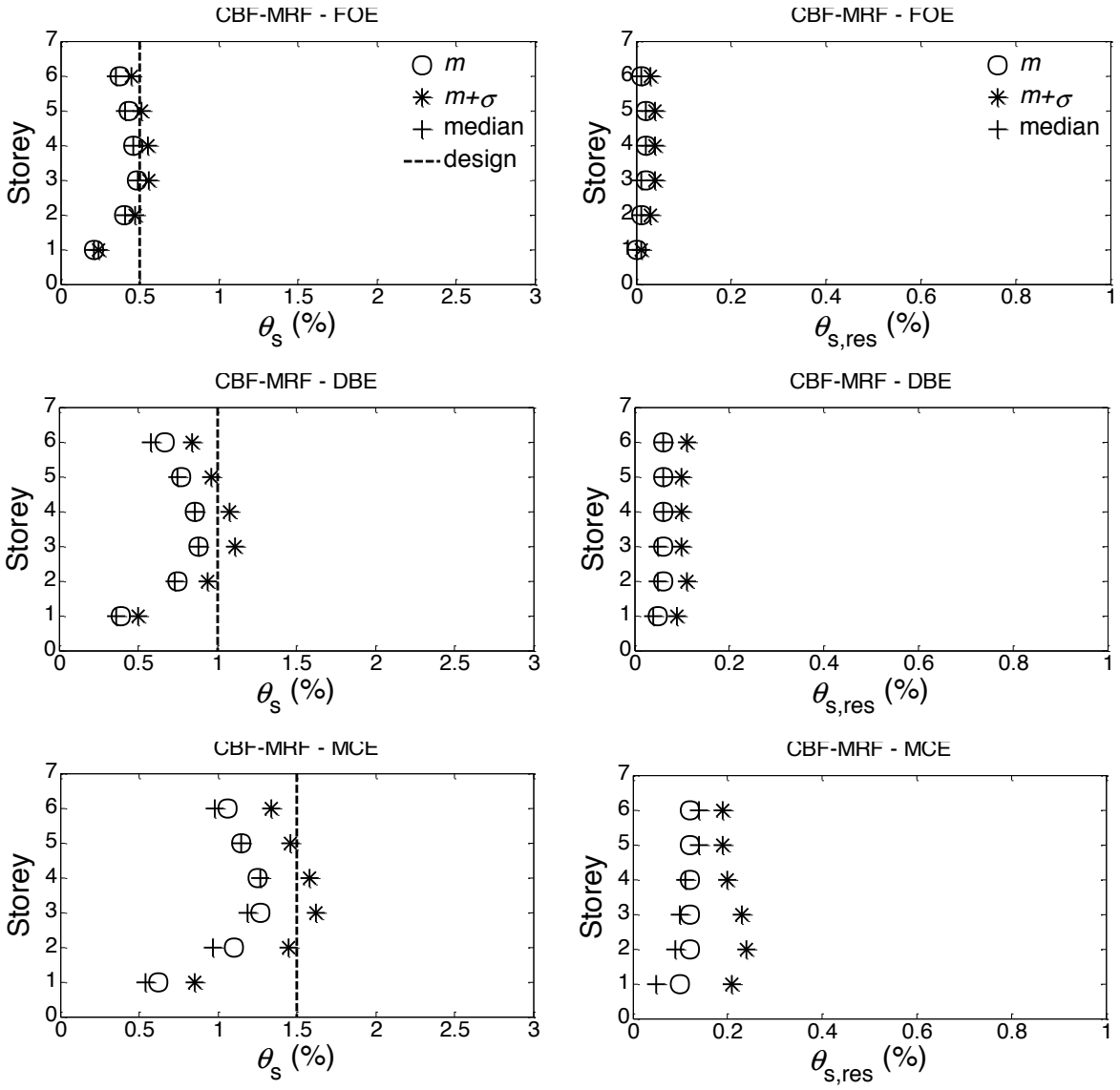

(a) (b)

Fig. 18. Response profiles of the CBF-MRF under 22 earthquake ground motions scaled to the FOE, DBE and MCE sesimic hazard levels: (a) peak storey drifts; and (b) residual storey drifts.

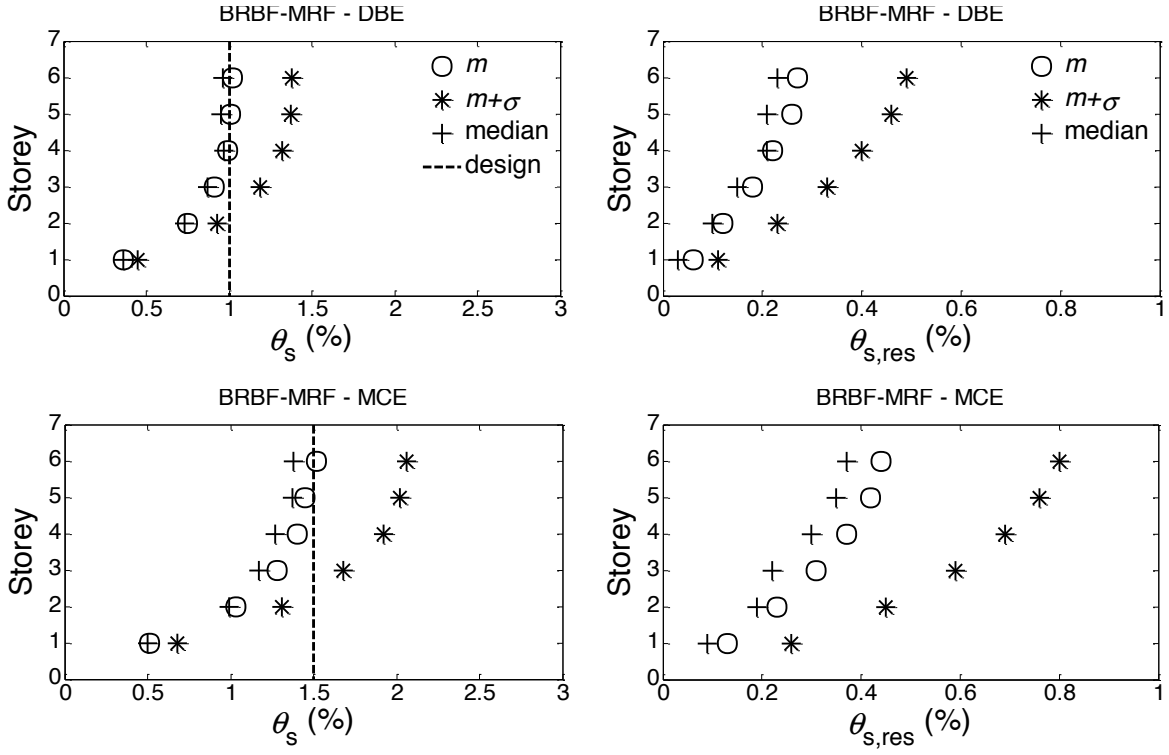

(a) (b)

Fig. 19. Response profiles of the BRBF-MRF under 22 earthquake ground motions scaled to the DBE and MCE sesimic hazard levels: (a) peak storey drifts; and (b) residual storey drifts.

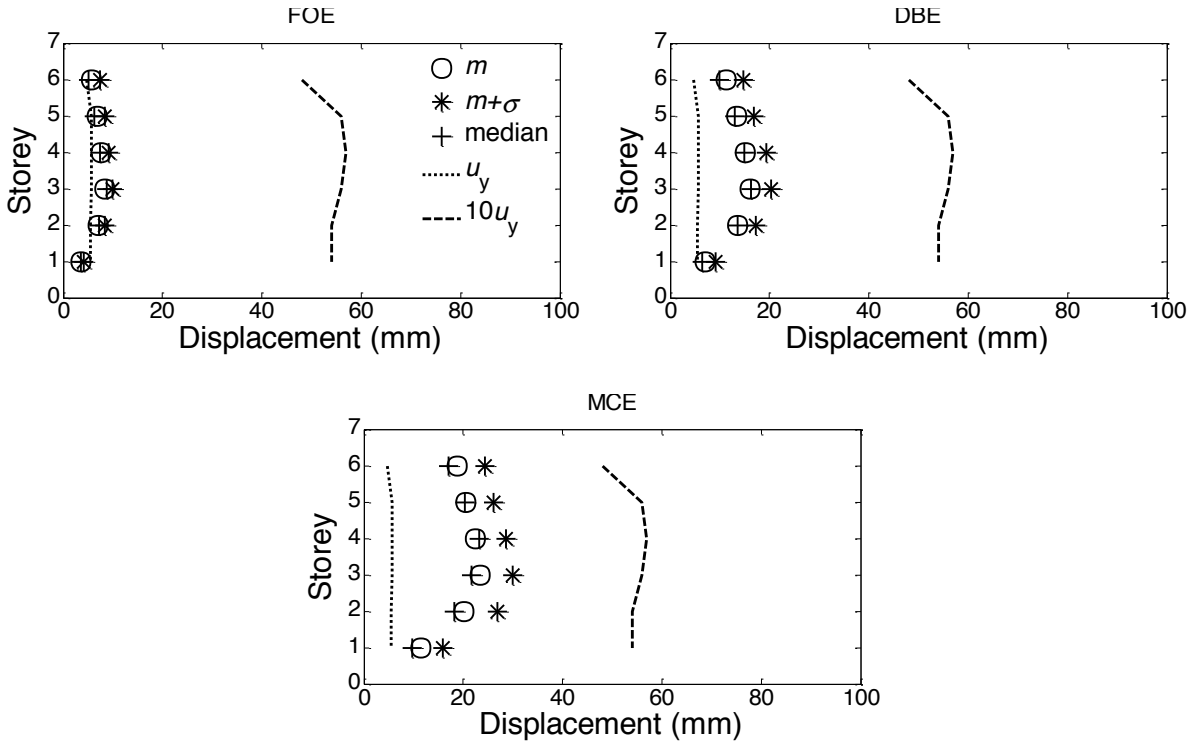

Fig. 20. Maximum displacements in SSD-WHPs under 22 earthquake ground motions scaled to the FOE, DBE and MCE sesimic hazard levels.

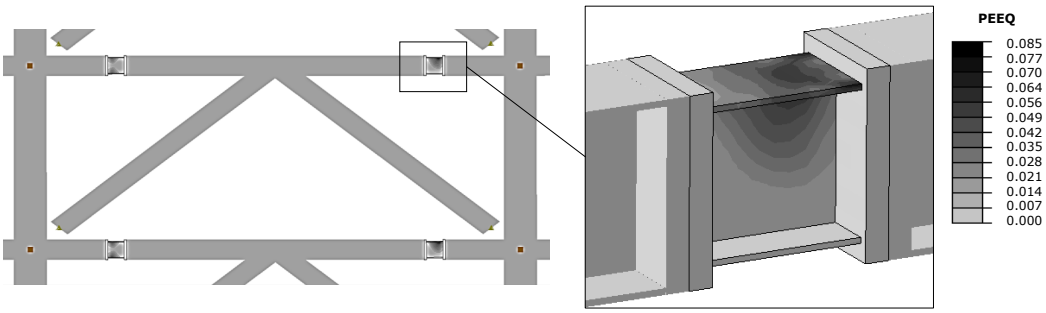

θ_r= 1.35%

Fig. 21. Equivalent plastic strain (PEEQ) distribution: beam-column connection with beam fuse under no. 16 record scaled to the MCE seismic hazard level (idealized beam element profiles are displayed).